Numerical simulation of a multilevel atom interferometer

B. Barrett,[1] I. Yavin,[2] S. Beattie,[1] and A. Kumarakrishnan[1]

[1]*Department of Physics & Astronomy, York University, Toronto, Ontario M3J 1P3, Canada*
[2]*Center of Cosmology & Particle Physics, New York University, New York, New York 10003, USA*

We present a comprehensive numerical simulation of an echo-type atom interferometer. The simulation confirms an interesting theoretical description of this interferometer that includes effects due to spontaneous emission and magnetic sublevels. Both the simulation and the theoretical model agree with the results of experiments. These developments provide an improved understanding of several observable effects. The evolution of state populations due to stimulated emission and absorption during the standing-wave interaction imparts a time-dependent phase on each atomic momentum state. This manifests itself as an asymmetry in the signal shape that depends on the strength of the interaction as well as spontaneous emission due to a nonzero population in the excited states. The degree of asymmetry is a measure of a nonzero relative phase between interfering momentum states.

PACS number(s): 37.25.+k, 37.10.Jk, 02.60.Cb, 03.75.−b

I. INTRODUCTION

In recent years, atom interferometers (AIs) have become an invaluable tool for a variety of experiments related to precision measurements and inertial sensing using cold atoms [1–13].

The echo-type AI used in this work [4,13–17] functions on the basis of phase modulation of the atomic wave function due to the interaction with standing-wave (sw) pulses. Although this phase modulation is directly connected to the recoil energy, its functional form has a complicated dependence on a number of mechanisms—such as the dynamic population of magnetic sublevels, phase shifts due to spontaneous and stimulated processes, and the excitation of multiple momentum states. Some of these mechanisms have been studied in previous works [14–16,18], but many aspects of the AI are not fully understood. In this work, we address all of these effects on the basis of a comprehensive numerical simulation and an improved analytical model.

The simulation presented here successfully models data using measured experimental parameters as inputs and completes our understanding of a broad class of observable effects. One such effect is an asymmetry in the shape of signals produced by the AI, which is a manifestation of a nonzero relative phase difference between interfering momentum states. We show that the level of asymmetry is related to the amount of spontaneous emission occurring during sw excitations, as well as stimulated processes such as Rabi flopping.

The analytical model of the AI accounts for effects due to both magnetic sublevels and spontaneous emission. By including these effects, we avoid the need for a phenomenological model that was previously used in measurements of the atomic recoil frequency [16]. Using this theoretical treatment, we are also able to estimate magnetic sublevel populations in the experiment.

Although the analytical model provides an improved understanding of the response of the AI, the model is still limited to short pulses such that the motion of the atom during the interaction can be ignored (Raman-Nath regime). Additionally, the model is limited to detunings (Δ) large compared to the Rabi frequency ($|\Delta| \gg \Omega_0$) and the spontaneous emission rate ($|\Delta| \gg \Gamma$). The analytical calculation also assumes that the

excited state adiabatically follows the ground state, eliminating any dynamic exchange of amplitude or phase between states. The decay of the excited state due to spontaneous emission is also accomplished in an approximate manner, since the ground-state amplitude is not repopulated by the excited state. As a result of these limitations, the theory fails to model experimental data accurately in several regimes of interest.

Since the simulation numerically solves the equations governing the system, none of the aforementioned limitations apply. The simulation accounts for the motion of atoms and the dynamic evolution of magnetic sublevel populations during the interaction with sw pulses, which is not a feature of the analytical calculation. In general, this approach allows for a much broader class of phenomena to be studied. Additionally, a precision measurement of the recoil frequency using this technique would involve a detailed study of systematic effects. This justifies the need for an accurate and robust model for the signal.

The rest of the article is organized as follows. Section II gives a brief description of the experiment. Section III reviews the main results pertaining to a theoretical calculation of the signal in two temperature regimes, one reminiscent of Bose-Einstein condensate (BEC) conditions involving one sw pulse and the other similar to conditions in a magneto-optical trap (MOT) involving two sw pulses. A detailed description of the calculation of the one-pulse recoil signal is given in the Appendix. In Sec. III, we also derive an expression for the signal that accounts for magnetic sublevels, which is used to model experimental data. In Sec. IV, we describe the theoretical background for the simulations. A discussion of the main results of this work follows in Sec. V. We present our conclusions in Sec. VI and discuss future directions and applications of this work.

II. DESCRIPTION OF EXPERIMENT

The AI is used to measure the two-photon atomic recoil frequency $\omega_q = \hbar q^2/2M$. Here, M is the mass of the atom and $\hbar q = 2\hbar k$ is the momentum transferred to the atom from counterpropagating laser fields with wavelength λ and wave
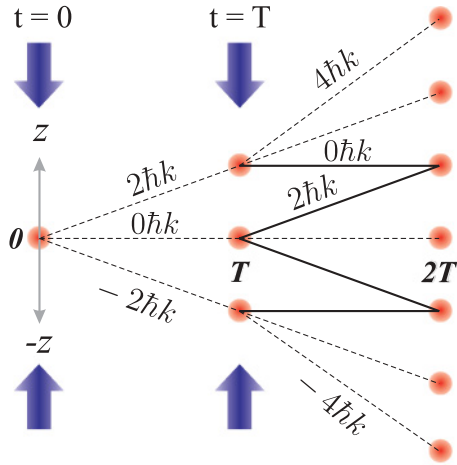
FIG. 1. (Color online) Recoil diagram for a time-domain atom interferometer. Center-of-mass momentum states are shown as red dots. The first sw pulse, applied at $t = 0$, diffracts the momentum states of the atom into multiples of the two-photon recoil momentum $2\hbar k$. The second sw pulse, applied at $t = T$, splits the momentum states further. Only the zeroth-order and $\pm$first-order diffractions from each sw pulse are drawn for simplicity. In the vicinity of the echo time, $t = 2T$, there is interference between all orders of momentum states. Our detection scheme is only sensitive to interferences between states that differ by $2\hbar k$. Two pairs of interfering momentum states are shown as solid black lines.
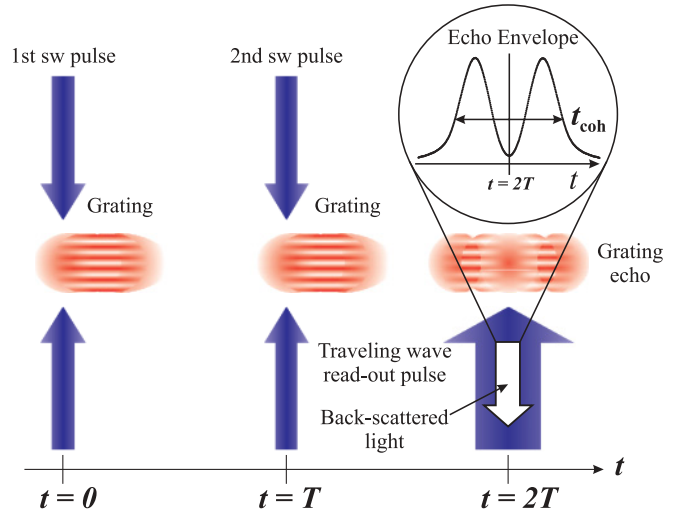

FIG. 2. (Color online) Pulse-timing diagram for the experiment. After each sw pulse, a modulation in atom density forms and then decays in a time $t_{coh} \sim 2/q\sigma_v$ due to Doppler dephasing. At time $t = 2T$, the grating echo forms as a result of the interference between different momentum states. A traveling wave readout pulse coherently backscatters light from the grating at this time. The intensity of this light is detected by a photomultiplier tube.

number $k = 2\pi/\lambda$. A sw laser pulse with off-resonant traveling wave components interacts with a sample of laser-cooled ^{85}Rb atoms (temperature $\mathcal{T} \sim 100~\mu$K) at times $t = 0$ and $t = T$. During each pulse, atoms complete several two-photon transitions corresponding to the absorption of a photon from one traveling wave component and stimulated emission into the oppositely directed traveling wave. This results in the diffraction of atoms into a superposition of momentum states separated by $\hbar q$, as shown in Fig. 1.

In the absence of spontaneous processes, and assuming both traveling wave components of the sw have the same polarization, the interaction returns the atoms to the same ground-state magnetic sublevel. The atomic wave function develops a phase modulation on a time scale $\tau_q = \pi/\omega_q \sim 32~\mu$s, where τ_q is referred to as the recoil period. This phase modulation evolves into a spatial and temporal modulation in the atomic density. Due to the finite velocity distribution of the atomic sample, the density grating dephases on a time scale defined by the coherence time $t_{coh} \sim 2/q\sigma_v \sim 1~\mu$s. Here, $\sigma_v \sim 10$ cm/s is the width of the velocity distribution. Since $t_{coh} \ll \tau_q$ for the conditions of our experiment, an echo technique is used to cancel the effect of Doppler dephasing and measure the temporal modulation induced on the density distribution due to atomic recoil. A second sw pulse, applied at $t = T$, causes interference of momentum states in the vicinity of the echo time, $t = 2T$, resulting in a rephasing of the density grating, as shown in Fig. 2. The grating contrast is measured by applying a traveling wave readout pulse (with the same wavelength as the sw pulses) and detecting the intensity of the coherently backscattered light from the atomic cloud. The density grating has various spatial harmonics in integer multiples of q due to the different orders of

interfering momentum states. However, due to the nature of Bragg diffraction, this detection technique is only sensitive to density modulation that has a spatial periodicity of $\lambda/2$ (spatial harmonic q)—the smallest grating spacing that can Bragg scatter light of wavelength λ. Only interfering momentum states that differ by $\hbar q$ can produce such a modulation. The integrated intensity of backscattered light (referred to as the echo intensity) is proportional to the contrast of the density grating. The echo intensity is a periodic function of the pulse separation, T, with period τ_q.

The experiment utilizes ^{85}Rb atoms cooled in a MOT contained within a glass vacuum system. The trap loads $\sim 10^9$ atoms in ~ 300 ms. Both the MOT laser beams and the magnetic field gradient are switched off prior to the AI experiment. The MOT B-field gradient is turned off in $\sim 100~\mu$s, after which the atoms are cooled in an optical molasses for several milliseconds. Three pairs of coils, one pair along each direction, are used to cancel residual magnetic fields and magnetic-field gradients. These coils remain on continuously. Under these conditions, the magnetic field at the time of the echo experiment is canceled at the level of 1 mG over the volume of the trap. The AI excitation pulses are derived from two off-resonant, circularly polarized, traveling wave beams. They are overlapped at the location of the trap to form a sw along the vertical direction. The AI beams have a Gaussian intensity profile and are collimated to a diameter of ~ 2 cm. All excitation pulses are produced by using digital delay generators to trigger acousto-optic switches. The backscattered light intensity from the grating is detected using a gated photomultiplier tube. Measurements of ω_q are accomplished by measuring the contrast of the grating as a function of the pulse separation, T, on a suitably long time scale. A more detailed description of the experiment is given in Ref. [15].

III. THEORY

The theoretical expression for the recoil signal was originally derived in Ref. [4]. The influence of magnetic sublevels was subsequently included for studies of nanostructures in cold atoms [14]. The treatment in Ref. [16] addressed the role of spontaneous emission on the recoil signal. In this work, we include both effects to develop a complete understanding of the properties of the recoil signal. Since theoretical derivations of this signal have been studied previously, we present the details in the Appendix. Here, we review the main results required to understand the recoil signal in the one-pulse regime (appropriate for BEC conditions) and the two-pulse regime (used for experiments under MOT conditions). These results are used as a foundation for developing numerical techniques and for testing the accuracy of simulations.

A. One-pulse recoil signal

The one-pulse regime assumes the velocity distribution of the sample is infinitely narrow. The calculation is carried out in three stages. In the first stage, the Schrödinger equation is solved for the ground-state amplitude of the atomic wave function, a_g, using the two-level Hamiltonian for a sw laser pulse of duration τ_1. The Hamiltonian assumes that the sw pulse is short (Raman-Nath regime) such that the motion of the atoms along the axis of the sw can be neglected during the interaction. This allows us to ignore the kinetic energy term in the Hamiltonian during the sw pulse. It also assumes that the pulse is far off-resonance ($|\Delta| \gg \Omega_0, \gamma$) such that the excited state is not significantly populated. Here, $\Delta \equiv \omega - \omega_0$ is the detuning of the laser frequency, ω, from the atomic resonance frequency, ω_0, $\Omega_0 \equiv \mu_{eg} E_0/\hbar$ is the Rabi frequency, μ_{eg} is a dipole matrix element, E_0 is the electric-field amplitude of each traveling wave component of the sw, and $\gamma = \Gamma/2$, where Γ is the spontaneous emission rate.

In the second stage of the calculation, after the pulse has turned off, the atom is allowed to evolve in free space for a time t, which results in a modification of the phase of the ground-state amplitude. In an experiment involving a BEC, a traveling wave readout pulse with wavelength λ can be applied to the atomic sample and the intensity of the backscattered electric field can be detected as the signal. The amplitude of the backscattered electric field is proportional to the $\lambda/2$-periodic component of the atomic density modulation (the $2k = q$ Fourier harmonic) produced by the sw interaction.

The final stage of the calculation requires a computation of the probability density of the ground state, $\rho_g(r,t)$. The recoil signal is obtained by evaluating the square of the q Fourier harmonic of this probability density.

The Hamiltonian in the field-interaction representation [19] for a two-level atom is

$$\tilde{\mathcal{H}} = \hbar \begin{pmatrix} -\Delta - i\gamma & \Omega(r) \\ \Omega(r) & 0 \end{pmatrix}, \tag{1}$$

where $\Omega(r) = \Omega_0 \cos(k \cdot r)$ for a sw laser field. The energy is defined to be zero for the ground state and $-\hbar\Delta$ for the excited state. The $-i\hbar\gamma$ term is a phenomenological constant added to account for spontaneous emission during the interaction, which gives rise to amplitude decay of the excited state. This approach is valid in any open two-level system, but only approximately accounts for spontaneous emission in a closed system since the excited state population is not fed into the ground state (normalization is not preserved). In addition, this Hamiltonian does not account for the atomic recoil due to the photon emission. By using the density matrix approach [20] or resorting to Monte-Carlo wave function techniques [21], a more complete model of spontaneous emission can be realized.

As shown in the Appendix, the amplitude of the backscattered electric field as a function of the time, t, after the sw pulse is

$$\tilde{E}_1(t) \propto -u_1 \sin(\omega_q t - \theta)[J_0(\kappa_1) + J_2(\kappa_1)], \tag{2}$$

where u_1 is the magnitude of the sw pulse area [Eq. (A4)], ω_q is the two-photon recoil frequency, θ is a parameter associated with spontaneous emission given by

$$\theta = \tan^{-1}\left(-\frac{\Gamma}{2\Delta}\right), \tag{3}$$

$J_\nu(x)$ is the νth-order Bessel function of the first kind, and κ_1 is given by Eq. (A13). From Eq. (2) it is clear that the field amplitude is proportional to u_1 in the small-pulse-area regime and is shifted by a phase θ due to spontaneous emission. This has interesting consequences for the signal shape and will be discussed in detail in Sec. V B 1.

For sufficiently cold atomic samples ($\sim$10 nK), $t_{\text{coh}} \gg \tau_q$ and Doppler dephasing is negligible, thereby allowing the temporal modulation in the contrast to be resolved after a single sw pulse [6]. The ground-state density after the interaction with the sw pulse [Eq. (A10)] is shown in Figs. 3(a) and 3(b) for low- and high-pulse areas, respectively, in the absence
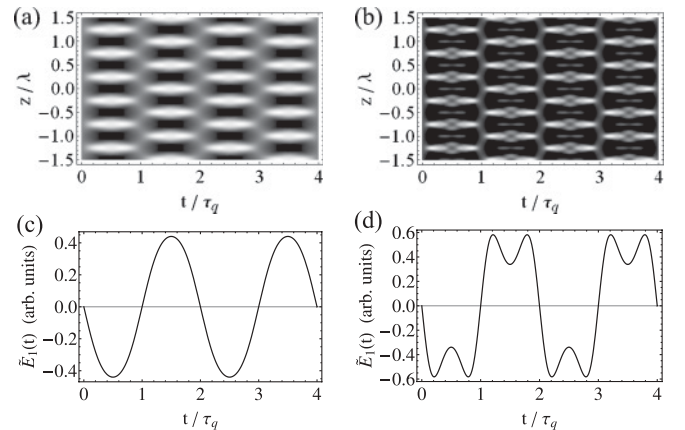

FIG. 3. Density distribution, $\rho_g(z,t)$, and corresponding backscattered electric field amplitude, $\tilde{E}_1(t)$, for an atomic sample after the interaction with a weak sw pulse (a,c) and a strong sw pulse (b,d). In plots (a) and (b), z is the distance along the sw field. Dark portions correspond to low density while light portions correspond to high density. $\rho_g(z,t)$ shows spatial modulation that is periodic at integer multiples of $\lambda/2$ and shows temporal modulation at integer multiples of twice the recoil frequency, $2\omega_q$, as the pulse area increases. Equation (A10) was used to produce plots (a) and (b) with first pulse area $u_1 = 0.5$ and 1.5, respectively. In plots (c) and (d), Eq. (2) was used with the same respective pulse areas. The zeros in the contrast of the density modulation correspond to the zeros in $\tilde{E}_1(t)$. The effects of spontaneous emission were ignored for all plots.

of spontaneous emission ($\theta = 0$). For small-pulse areas, the density is sinusoidally modulated in space with a period $\lambda/2$. The contrast of this spatial modulation oscillates in time with a period τ_q, as shown in Fig. 3(a). This density distribution corresponds to the momentum state $|\boldsymbol{p} = 0\rangle$ interfering with the $|\boldsymbol{p} = \pm\hbar\boldsymbol{q}\rangle$ states. For higher-pulse areas, the density distribution becomes more complicated [as shown in Fig. 3(a)] due to the presence of additional spatial harmonics from the interference of higher-order momentum states. The temporal modulation of the contrast also exhibits higher-order harmonics but still primarily oscillates at the fundamental frequency $2\omega_q$.

The amplitude of the backscattered field, $\tilde{E}_1(t)$ [Eq. (2)], derived from the ground-state density $\rho_g(z,t)$ given by Eq. (A10), is shown in Figs. 3(c) and 3(d) for the same pulse areas. The field changes with time due to the oscillations in the contrast of the density distribution. For small u_1, only the lowest-order momentum states contribute to the signal, and $\tilde{E}_1(t)$ oscillates sinusoidally at frequency ω_q. In general, the states $|n\hbar\boldsymbol{q}\rangle$ and $|(n+1)\hbar\boldsymbol{q}\rangle$ interfere to produce a $\lambda/2$ spatial modulation with a contrast that oscillates in time with a frequency $2(2n+1)\omega_q$. For higher-pulse areas, additional harmonics in the density distribution give rise to the shape of the backscattered field shown in Fig. 3(d). Equation (2) takes into account the interference of any two p states differing by $\hbar\boldsymbol{q}$ in momentum, but no higher-order interferences—for example, between $|n\hbar\boldsymbol{q}\rangle$ and $|(n+2)\hbar\boldsymbol{q}\rangle$.

The analytical expression for the one-pulse recoil signal, denoted by $\tilde{s}_1$, is simply the intensity of the backscattered field: $\tilde{s}_1(t) \propto |\tilde{E}_1(t)|^2$. This quantity is proportional to the contrast of the density modulation.

B. Two-pulse recoil signal

The theoretical expression of the recoil signal in the two-pulse regime is a simple extension of that in the one-pulse regime. Typically, the two-pulse experiment is carried out under MOT conditions where Doppler dephasing becomes important because the velocity distribution of the atoms can no longer be approximated by a δ function.

As shown in the Appendix, the sw interaction is equivalent to a phase grating in diffractive optics. The calculation for the two-pulse recoil signal involves applying an additional phase grating $e^{i\Theta_2 \cos(q \cdot r)}$, associated with the second sw pulse, to the atomic wave function a time $t = T$ after the first pulse [shown in Eq. (A9)]. The atom evolves in free space after the second pulse until a time $t_{\text{echo}}^{(N)} = (N+1)T$, called the Nth-order echo time, where the Doppler phases from all velocity classes cancel. Here, $N = \eta/\zeta$, where η is the momentum difference between interfering p states from the first pulse (in units of $\hbar\boldsymbol{q}$) and ζ is the equivalent quantity for the second pulse. When averaged over the velocity distribution, the atomic density shows modulation with a nonzero contrast only in the vicinity of these echo times. At all other times, the density is uniform since the modulation has been washed out by Doppler dephasing. In the general case, N is a rational number [14,19], but in our case we consider only the first-order echo which occurs at time $t_{\text{echo}}^{(1)} = 2T$, corresponding to $N = 1$. The density of the atomic sample after the two sw pulses and at the first-order echo time is depicted in Fig. 2.

The amplitude of the backscattered electric field about $t = 2T$ can be shown to be

$$\langle \tilde{E}_2(\Delta t, T) \rangle \propto \tilde{E}_1(\Delta t) e^{-(\Delta t/t_{\text{coh}})^2} \frac{u_2^2}{2} \sin^2[\omega_q(T + \Delta t) - \theta]$$
$$\times \left[J_0(\kappa_2) + \frac{4}{3} J_2(\kappa_2) + \frac{1}{3} J_4(\kappa_2) \right], \quad (4)$$

where T is the separation between sw pulses, $\Delta t = t - 2T$ is the time relative to the echo time, u_2 is the magnitude of the second pulse area, and

$$\kappa_2 \equiv 2u_2\sqrt{\sin[\omega_q(T + \Delta t) - \theta]\sin[\omega_q(T + \Delta t) + \theta]}. \quad (5)$$

The $\langle \cdots \rangle$ brackets in Eq. (4) indicate that the backscattered field has been averaged over the initial velocity distribution, which is assumed to be Maxwellian with a characteristic width $\sigma_v = \sqrt{2k_B\mathcal{T}/M}$, which is also equal to the most probable speed. The coherence time, $t_{\text{coh}} = 2/q\sigma_v$, is the time about the echo time for which the backscattered field is nonzero and is determined solely by σ_v.

From Eq. (4), which is equivalent to Eq. (25) in Ref. [16], it is clear that for small u_2 the basic signal dependence on pulse separation, T, is a sinusoidal oscillation at frequency ω_q that is phase shifted by an amount θ [Eq. (3)]. This phase shift is associated with spontaneous emission. As the second pulse area becomes large, the third factor in Eq. (4) has a more significant contribution to the signal. This is associated with the interference of higher-order momentum states, as discussed in Sec. III A.

The two-pulse recoil signal is the integrated intensity of the backscattered light in the vicinity of the echo time. The Δt-integrated intensity is approximately proportional to the square of the T-dependent part of $\tilde{E}_2$ from Eq. (4):

$$\tilde{s}_2(T) \sim \frac{u_2^4}{4} \sin^4[\omega_q(T + \Delta t) - \theta]$$
$$\times \left[J_0(\kappa_2) + \frac{4}{3} J_2(\kappa_2) + \frac{1}{3} J_4(\kappa_2) \right]^2. \quad (6)$$

As a function T, this expression is periodic with fundamental frequency $2\omega_q$ (period $\tau_q = \pi/\omega_q \sim 32$ μs). The signal, $\tilde{s}_2$, is proportional to the grating contrast measured in the experiment, which is a manifestation of phase modulation in the atomic wave function following the interaction with two sw pulses. The response of the AI depends on the level structure of the atom and the coupling between these levels and the driving field. We now explore these effects in detail.

C. Recoil signal including magnetic sublevels

So far, we have reviewed the theoretical expressions for the one- and two-pulse recoil signals, including the effects of spontaneous emission, for a two-level atom. In the experiment we use ^{85}Rb, which is a multilevel atom. If only the $F = 3 \rightarrow F' = 4$ transition is considered, there are $2F + 1 = 7$ ground-state magnetic sublevels and 9 excited-state sublevels. These energetically degenerate sublevels play a significant role in the response of the AI. A previous treatment of the two-pulse signal [14] accounted for multiple atomic levels but assumed the population was equally distributed and ignored effects due to spontaneous emission. Here we

extend the theoretical model of the recoil signal discussed in the previous two subsections to include multilevel atoms with an arbitrary distribution of initial sublevel populations.

The coupling strength between states $|g\rangle = |n_g J_g m_g\rangle$ and $|e\rangle = |n_e J_e m_e\rangle$ is determined by the dipole matrix element

$$\mu_{eg} = -e \langle e| \hat{\epsilon}_{q_L} \cdot \boldsymbol{r} |g\rangle = -e\langle n_e J_e \|r\| n_g J_g\rangle C^{J_g \ 1 \ J_e}_{m_g \ q_L \ m_e}, \quad (7)$$

where n_g, n_e are the principal quantum numbers, J_g, J_e are the total angular momenta, and m_g, m_e are the magnetic sublevels of the ground and excited states, respectively. In our case, $J_g = F = 3$ and $J_e = F' = 4$. The unit vector $\hat{\epsilon}_{q_L}$ represents the polarization of the laser field. Linear and circular polarization states are denoted by q_L ($q_L = 0$ for linear and $q_L = \pm 1$ for $\sigma^\pm$ polarizations). The factor $\langle n_e J_e \|r\| n_g J_g\rangle$ in Eq. (7) is the reduced matrix element associated with the radial part of the wave functions—the magnitude of which is unimportant for this treatment and will be absorbed into the Rabi frequency, $\Omega_0 = \mu_{eg} E_0/\hbar$. The factor $C^{J_g \ 1 \ J_e}_{m_g \ q_L \ m_e}$ is the Clebsch-Gordan coefficient, which describes how strongly two states are coupled by the photon and depends on the particular transition. Since we are only concerned with electric dipole transitions, it is nonzero only for states that obey the selection rules: $J_e = J_g + 1$ and $m_e = m_g + q_L$.

From Eq. (7), it is apparent that each degenerate m level interacts with a sw pulse (of a given polarization) with a different coupling strength—which is proportional to the Rabi frequency for each transition: $C^{J_g \ 1 \ J_e}_{m_g \ q_L \ m_e} \Omega_0$. In the experiment, this differential coupling causes the population of the m levels to become unbalanced after the interaction with the sw pulse (optical pumping). The degree of the imbalance is determined by Ω_0, Δ, and the pulse durations. In the analytical treatment that follows, optical pumping is not taken into account. We assume the population of each m level remains constant during the sw pulses. However, the numerical simulation to be discussed in Sec. IV includes optical pumping effects.

The area of a given sw pulse, denoted by index $j = 1$ or 2, is given by

$$u_j^{(m_g)} = \frac{\Omega_0^2 \tau_j}{2\Delta} \left[1 + \left(\frac{\Gamma}{2\Delta} \right)^2 \right]^{-1/2} \left(C^{J_g \ 1 \ J_e}_{m_g \ q_L \ m_e} \right)^2, \quad (8)$$

where τ_j is the pulse duration. For the one-pulse and two-pulse signals, the backscattered field amplitude from the state $|J_g m_g\rangle$ is

$$\tilde{E}_1^{(m_g)}(t) \propto u_1^{(m_g)} \left(C^{J_g \ 1 \ J_e}_{m_g \ q_L \ m_e} \right)^2$$
$$\times \sin(\omega_q t - \theta) \left[J_0(\kappa_1) + J_2(\kappa_1) \right], \quad (9a)$$
$$\langle \tilde{E}_2^{(m_g)}(T) \rangle \propto \frac{1}{2} \left(u_2^{(m_g)} \right)^2 \left(C^{J_g \ 1 \ J_e}_{m_g \ q_L \ m_e} \right)^2$$
$$\times \sin^2[\omega_q(T + \Delta t) - \theta]$$
$$\times \left[J_0(\kappa_2) + \tfrac{4}{3} J_2(\kappa_2) + \tfrac{1}{3} J_4(\kappa_2) \right]. \quad (9b)$$

Here it is understood that u_1 in Eq. (A13) for κ_1 (for a two-level atom) has been replaced by $u_1^{(m_g)}$ for the multilevel case. Similarly, u_2 in Eq. (5) for κ_2 has been replaced by $u_2^{(m_g)}$. The extra factor of $(C^{J_g \ 1 \ J_e}_{m_g \ q_L \ m_e})^2$ in Eqs. (9) arises due to the coupling of states $|J_g m_g\rangle$ and $|J_e m_e\rangle$ by the traveling wave readout pulse (assuming that the scattered field has the same polarization as
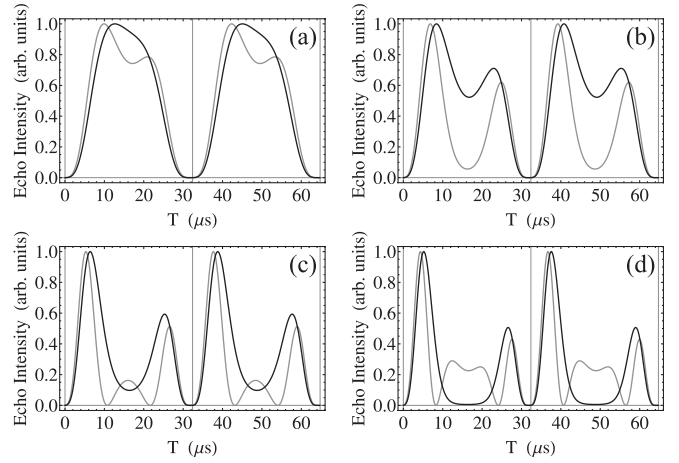

FIG. 4. Comparison of two-pulse recoil curves predicted by the two-level theory [Eq. (6), gray curve] and the theory including magnetic sublevels [square of Eq. (10b), black curve] for various second-pulse durations, τ_2 (a, 150 ns; b, 200 ns; c, 250 ns; d, 300 ns). Here the m-level populations were assumed to be equally distributed among the seven levels of the $J_g = 3$ ground state. Pulse parameters: $\Delta = 10\Gamma_N$, $\Omega_0 = 2.5\Gamma_N$, $\Gamma = \Gamma_N$.

the readout pulse). The total scattered field from the atom is proportional to the sum of the fields scattered by each m level weighted by the final population of that level, $\Pi_{J_g m_g}$:

$$\tilde{E}_1(t) \propto \sum_{m_g} \Pi_{J_g m_g} \tilde{E}_1^{(m_g)}(t) \quad (10a)$$

$$\langle \tilde{E}_2(T) \rangle \propto \sum_{m_g} \Pi_{J_g m_g} \langle \tilde{E}_2^{(m_g)}(T) \rangle. \quad (10b)$$

The one- and two-pulse recoil signals are proportional to the square of the total backscattered field amplitudes given by Eqs. (10) ($\tilde{s}_j \propto |\tilde{E}_j|^2$, for index $j = 1,2$). The form of Eqs. (10) allows for interference between scattered fields from each m level. This additional interference from magnetic sublevels strongly affects the shape of the recoil signal. Figure 4 shows a comparison of two-pulse recoil signals predicted by the two-level theory [Eq. (6)] and the theory including multiple sublevels [square of Eq. (10b)] for various second-pulse durations, τ_2. The two-level theory predicts extra zeros in the signal shape that are not observed experimentally. For the same set of pulse parameters, the multilevel theory does not predict these extra zeros due to the interference of backscattered light from each magnetic sublevel. The multilevel theory models experimental data much more effectively than all previous models, as we show in Sec. V A.

IV. DESCRIPTION OF SIMULATION

The main goal of the simulation is to compute the two-pulse recoil signal (scattered field intensity as a function of pulse separation, T) under the conditions of the experiment. In practice, the signal in the experiment is obtained from a macroscopic sample (typically $\sim 10^9$ atoms) at a temperature of $\mathcal{T} \sim 100 \, \mu$K. The most basic assumption of the simulation is that the signal from the AI can, in principle, be produced by a single atom. Instead of velocity averaging over many atoms with a well-defined momentum, as in the theoretical

calculation of the two-pulse recoil signal, the simulation solves for the time evolution of a single atom (represented by a wave packet in momentum space) with a Maxwell-Boltzmann probability distribution of velocities corresponding to a given temperature.

The theoretical framework of the simulation uses the Schrödinger picture to account for a number of physical effects, such as the motion of the atom at all times during the evolution; the bandwidth of sw pulses; Doppler shifts of momentum states; momentum-state excitation for arbitrary sw pulse duration, field strength, and detuning; population and coherence transfer between ground and excited states; population dissipation due to spontaneous emission; and optical pumping of magnetic sublevels.

We solve for the time-dependent state amplitudes of the atomic wave function. The computational cost of this problem scales as N_p multiplied by the number of time steps used, where N_p is the number of discrete momentum states. This is much less computationally expensive than the Heisenberg approach, where an $N_p \times N_p$ density matrix must be computed at every time step. However, the Heisenberg approach allows for a much broader class of problems to be addressed, such as the atomic recoil due to spontaneous emission [19] or N-atom effects such as collective excitation and emission of radiation. Similarly, a Monte-Carlo wave function (MCWF) approach in the Schrödinger picture would allow for a more complete model of spontaneous emission [21,22] with additional computational cost. In other work [15], we carried out MCWF simulations of sw pulses to study the excitation of momentum states and their relative populations for comparison with an experiment. In the case of the two-pulse recoil experiment, we found that the random photon recoil due to spontaneous emission has a negligible effect on the signal shape compared to the excited-state population damping associated with spontaneous emission. As a result, the photon recoil associated with spontaneous emission is not taken into account in the treatment presented here.

We now review the theoretical framework of the simulation. We restrict our model to atoms with two manifolds of energetically degenerate magnetic sublevels and total ground (excited)-state angular momentum J_g ($J_e = J_g + 1$). We label the states of the atom as $|J_g m_g\rangle$ and $|J_e m_e\rangle$. The Schrödinger equation is solved numerically in momentum space for wave functions in the field-interaction representation under the influence of an off-resonant, time-dependent sw potential. The Hamiltonian for this system in the rotating wave and dipole approximations is [19]

$$\mathcal{H} = \frac{\hat{P}_z^2}{2M} + \frac{\hbar}{2}\left(\Delta - \frac{kP_z}{M}\right)(\hat{S}_{J_g} - \hat{S}_{J_e}) + \frac{\hbar\Omega(t)}{2}$$
$$\times (|p - \hbar k\rangle\langle p| + |p + \hbar k\rangle\langle p|)(\hat{S}_{q_L}^+ + \hat{S}_{q_L}^-). \quad (11)$$

Here $\hat{P}_z$ is the momentum operator along the z axis, $\Delta \equiv \omega - \omega_0$ is the detuning of the laser field from resonance, $\hat{S}_{J_g} = |J_g\rangle\langle J_g|$ ($\hat{S}_{J_e} = |J_e\rangle\langle J_e|$) is the ground (excited)-state projection operator, $\Omega(t) = \mu E_0 \mathcal{E}(t)/\hbar$ is the (time-dependent) Rabi frequency with envelope function $\mathcal{E}(t)$, $|p \pm \hbar k\rangle\langle p|$ are raising and lowering operators for the momentum state $|p\rangle$ in units of the photon momentum, and $\hat{S}_{q_L}^+$ ($\hat{S}_{q_L}^-$) is a raising (lowering) operator proportional to the atomic dipole operator for laser

field polarization state q_L. These operators are defined as follows:

$$\hat{S}_{q_L}^+|J_g m_g\rangle = C_{m_g \, q_L \, m_g+q_L}^{J_g \, 1 \, J_e}|J_e \, m_g + q_L\rangle, \quad (12a)$$

$$\hat{S}_{q_L}^-|J_e m_e\rangle = C_{m_e \, q_L \, m_e-q_L}^{J_e \, 1 \, J_g}|J_g \, m_e - q_L\rangle, \quad (12b)$$

$$\hat{S}_{q_L}^+|J_e m_e\rangle = \hat{S}_{q_L}^-|J_g m_g\rangle = 0. \quad (12c)$$

Clebsch-Gordan coefficients, $C_{m_1 \, m_2 \, M}^{j_1 \, j_2 \, J}$, describe the coupling of different ground- and excited-state m levels. The pulse envelope, $\mathcal{E}(t)$, is based on a sum of exponential functions of the form $1/(1 + e^{-x})$, where $x = (t - t_0)/\tau_{\rm rise}$ for the rising edge of the pulse at time $t = t_0$, $x = -(t - t_1)/\tau_{\rm rise}$ for the falling edge at $t = t_1$, and $\tau_{\rm rise}$ is the rise time. Typically, the rise time is set equal to the experimentally measured value of 20 ns. The duration of the pulse is defined as $\tau = t_1 - t_0$.

The total momentum space wave function, $\Phi(p,t)$, can be written as a linear combination of the $2J_g + 1$ ground states $|J_g m_g\rangle$ and the $2J_e + 1$ excited states $|J_e m_e\rangle$,

$$\Phi(p,t) = \sum_{m_g} \alpha_{J_g m_g}(p,t)|J_g m_g\rangle + \sum_{m_e} \beta_{J_e m_e}(p,t)|J_e m_e\rangle,$$
$$(13)$$

where $\alpha_{J_g m_g}$ and $\beta_{J_e m_e}$ are the corresponding state amplitudes.

The main goal of the simulation is to find the state amplitudes that simultaneously satisfy the Schrödinger equation and the set of rate equations that describe spontaneous emission. The solution to the Schrödinger equation is computed using a combination of two methods. When the interaction potential is turned off [i.e., $\mathcal{E}(t) = 0$] and the excited state population $(\Pi_{J_e}(t))$ is zero, an analytical solution of the Schrödinger equation in free space is used to compute $\Phi(p,t)$. At all other times, the solution is computed using a fourth-order Runge-Kutta routine [23]. To describe spontaneous transitions from the excited to ground levels, the numerical solver also simultaneously satisfies the following rate equations for the m-level populations:

$$\dot{\Pi}_{J_e m_e} = -\Gamma \Pi_{J_e m_e}, \quad (14a)$$

$$\dot{\Pi}_{J_g m_g} = \sum_{q_L} \left(C_{m_g \, q_L \, m_g+q_L}^{J_g \, 1 \, J_e}\right)^2 \Gamma \Pi_{J_e m_g+q_L}. \quad (14b)$$

These equations have a solution:

$$\Pi_{J_e m_e}(t') = \Pi_{J_e m_e}(t)e^{-\Gamma(t'-t)}, \quad (15a)$$

$$\Pi_{J_g m_g}(t') = \Pi_{J_g m_g}(t) + (1 - e^{-\Gamma(t'-t)})$$
$$\times \sum_{q_L} \left(C_{m_g \, q_L \, m_g+q_L}^{J_g \, 1 \, J_e}\right)^2 \Pi_{J_e m_g+q_L}(t). \quad (15b)$$

Typically, $\Gamma = \Gamma_N = 3.76 \times 10^7$ s^{-1}, which is the natural radiative rate of the $5^2 P_{3/2}$ excited state for ^{85}Rb [24].

Figure 5 shows the evolution of m-level populations in the ground level during a sw pulse for (a) circular and (b) linear polarizations. Here, the initial populations are equally distributed among the seven sublevels. Evidence of optical pumping is clearly visible after only $\tau_1 \sim 300$ ns, which is the typical duration of sw pulses in the experiment.

The initial ground-state population, $\Pi_{J_g}(0)$, is set to unity and the code ensures that the normalization of the wave function is preserved for all times thereafter. The population
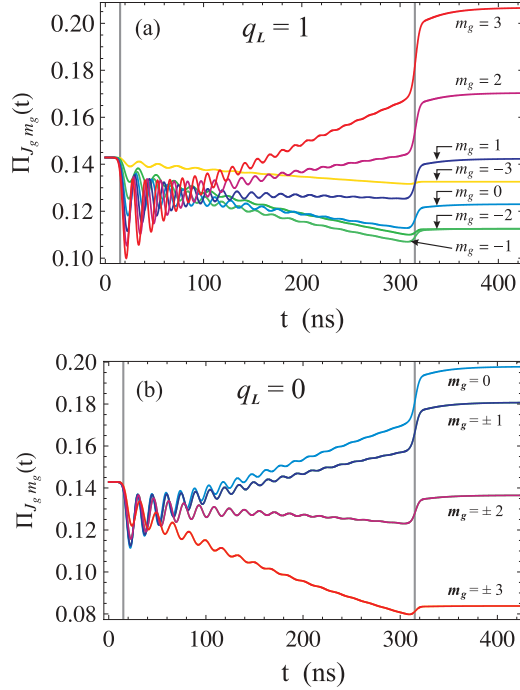
FIG. 5. (Color online) Evolution of ground-state magnetic sublevel populations during a sw pulse for (a) σ^+ and (b) linear polarization states. The vertical gray grid lines in each plot indicate where the sw pulse turns on and off. For circular polarization there is optical pumping toward the $m_g = 3$ level, while for linear polarization the population is pumped toward the $m_g = 0$ level. Pulse parameters: $\tau_1 = 300$ ns, $\tau_{\text{rise}} = 20$ ns, $\Delta = 8.36\Gamma_N$, $\Omega_0 = 5\Gamma_N$, $\Gamma = \Gamma_N$.

of a particular manifold at any time, $\Pi_J(t)$, is the sum over all m-level populations, $\Pi_{Jm}(t)$, in that manifold and is related to the state amplitude, $\alpha_{Jm}(p,t)$, through the following expressions:

$$\Pi_{J_g}(t) = \sum_{m_g} \Pi_{J_g m_g}(t) = 1 - \Pi_{J_e}(t), \qquad (16a)$$

$$\Pi_{J_g m_g}(t) = \int \left| \alpha_{J_g m_g}(p,t) \right|^2 dp. \qquad (16b)$$

To account for the finite velocity distribution of the laser-cooled sample, we use a Gaussian wave packet to describe the initial momentum distribution of each magnetic sublevel. The initial wave function can be written as

$$\Phi(p,0) = \sum_{m_g} \alpha_{J_g m_g}(p,0) |J_g\, m_g\rangle, \qquad (17a)$$

$$\alpha_{J_g m_g}(p,0) = \alpha_{J_g m_g}(0) \left[\frac{e^{-(p-p_0)^2/2\sigma_p^2}}{\sqrt{2\pi}\sigma_p} \right]^{1/2}. \qquad (17b)$$

Here, p_0 is the average initial momentum, $\sigma_p = \hbar/\Lambda$ is the standard deviation of the p-space probability distribution, and $\Lambda = h/(2\pi M k_B \mathcal{T})^{1/2}$ is the thermal de Broglie wavelength. The coefficients $\alpha_{J_g m_g}(0)$ are free parameters that define the initial population of each ground-state m level.

For the one-pulse recoil signal, the backscattered field from each m level is computed using the amplitude of the q Fourier harmonic from each ground-state amplitude, as given by

$$E_1^{(m_g)}(t) \propto \left(C_{m_g\ q_L\ m_e}^{J_g\ 1\ J_e} \right)^2 \int \alpha_{J_g m_g}^*(p,t) \alpha_{J_g m_g}(p - \hbar q, t)\, dp. \qquad (18)$$

This expression is analogous to Eq. (9a) in the analytical model. The total backscattered field is a sum over the scattered fields from each m level:

$$E_1(t) = \sum_{m_g} E_1^{(m_g)}(t). \qquad (19)$$

No m-level population factors appear in Eq. (19), as they do in the analytical equivalent [Eq. (10a)], because the populations are intrinsically built into the state amplitudes, $\alpha_{J_g m_g}$, that appear in Eq. (18). The one-pulse recoil signal is then $s_1(t) = |E_1(t)|^2$, where t is the time after the sw pulse. From Eq. (19), it is evident that the shape of the recoil signal depends on the distribution of initial ground-state amplitudes, $\alpha_{J_g m_g}(0)$.

In the two-pulse regime we use a temperature of $\sim 50\ \mu$K, which is 5000 times larger than that used in the one-pulse regime, but a factor of ~ 2 smaller than the typical temperature in the experiment. This is done to reduce the computation time in the two-pulse regime. We use a similar method to compute the intensity of the backscattered field as in the two-pulse experiment. In the vicinity of the grating echo the intensity is $|E_1(2T + t')|^2$, where t' is the time relative to $t = 2T$ and E_1 is given by Eq. (19). Therefore, we calculate the two-pulse recoil signal by integrating this quantity over t', as given by

$$s_2(T) = \int |E_1(2T + t')|^2 dt'. \qquad (20)$$

This quantity is analogous to the expression for the two-pulse recoil signal for a two-level system [Eq. (6)] or for an m-level system [square of Eq. (10b)].

To conclude the description of the simulations, we discuss the discretization of momentum space. In the two-pulse regime, the width of the wave function is $\sigma_p \sim 5\hbar k$. The discretization size is then typically set to $\Delta p \sim \sigma_p/250 \sim \hbar k/50$ for good p-space resolution. However, due to the reduced temperature in the one-pulse regime, the width of the wave function is much smaller ($\sigma_p \sim 0.01\hbar k$—much less than the $\hbar k$ transferred by absorption or emission along z). Hence, we can use $\Delta p = \hbar k$ since this is the smallest momentum transfer allowed by the sw interaction.

The number of sw pulses and the p-space discretization size has a large effect on the computational cost of the simulation in the two regimes. Since the two-pulse regime requires an additional sw pulse, a smaller Δp, and the evaluation of the signal is carried out as a function of T, it is much more computationally demanding than the one-pulse regime. Typically, the computation time is ~ 12 h for the two-pulse regime and ~ 30 s for the one-pulse regime on a computing network using 2.2-GHz processors (SHARCNET). However, the underlying physics in both regimes is essentially the same and many features of the two-pulse recoil signal can be studied using one-pulse simulations.

V. RESULTS AND DISCUSSION

Here we discuss the two main results of this work: the effects on the recoil signal due to magnetic sublevels and the momentum-dependent phase imprinted on the ground state by spontaneous and stimulated processes. We also present a detailed description of the mechanisms that contribute to the shape of the signal.

A. Effects due to magnetic sublevels

Figure 6 shows data from the two-pulse recoil experiment for various second sw pulse durations, τ_2. The echo intensity was recorded as a function of the pulse separation, T, for circularly polarized sw pulses ($|q_L| = 1$). Particular values of τ_2 (70, 86, and 98 ns) were chosen to illustrate a range of signal shapes typically observed in the experiment. Two separate fits to the data are shown, one based on the two-level model [Eq. (6)] and the other on the multilevel model [square of Eq. (10b)]. The two-level theory is insufficient for accurately modeling experimental data, whereas the multilevel theory fits all aspects of the signal for a large range of shapes. In particular, the multilevel theory successfully models the asymmetry and the broad valleys between zeros of the signal that occur as the area of the second pulse is increased, as shown in Fig. 6. Fits using the multilevel theory show a factor of $\sim$10 improvement in the χ^2/(degrees of freedom) compared to that of the two-level theory, which corresponds to a factor of $\sim$3 improvement in the relative uncertainty of the recoil frequency. Thus, the multilevel model is ideally suited for precision measurements of ω_q using this technique.

The development of this multilevel model—which contains only measurable parameters—represents a significant improvement in our understanding of the AI since previous efforts [16] relied upon a phenomenological model to fit experimental data. This model was unable to explain the underlying physical mechanisms that govern the signal shape. Additionally, the present model is far more successful in fitting the full range of signal shapes that can be generated in the experiment compared to the phenomenological model.

Another complication in modeling the AI is that magnetic sublevels and the spatial intensity profile of the excitation beams can be shown to produce similar effects on the signal shape. In this work, the beam diameter ($\sim$2 cm) was larger than the diameter of the atomic cloud ($\sim$1 cm). Therefore, we were able to demonstrate conclusively that magnetic sublevels played the dominant role in the response of the AI.

The data shown in Fig. 6 validate the multilevel model developed in Sec. III C. A distribution of populations among several ground-state magnetic sublevels smears out any extra zeros in the signal that would occur if the system were optically pumped into a single state, for example $|J_g J_g\rangle$. This smearing is due to interference between the coherently scattered light from each m level. Additionally, the valleys between the zeros in the signal are significantly broadened. These effects are most prominent when the pulse areas (u_1 and u_2) are large, since (i) higher-order momentum states are contributing to the signal from each m level (resulting in the double-peaked shape) and (ii) population imbalance in the m levels is maximized.
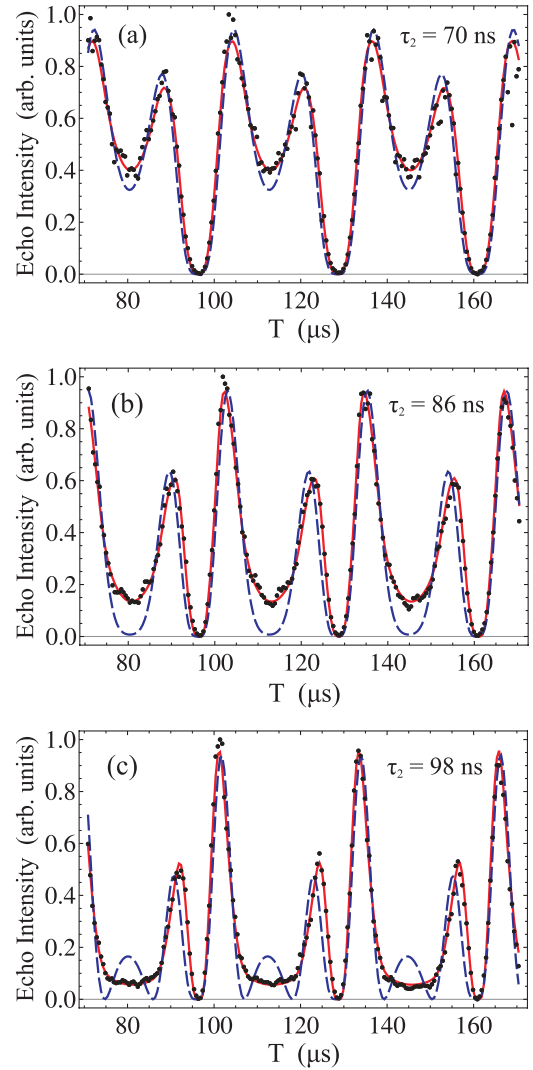

FIG. 6. (Color online) Data from the two-pulse recoil experiment for different second-pulse durations, τ_2 (a, 70 ns; b, 86 ns; c, 98 ns). Data is fit to the two-level expression [Eq. (6)] shown as the blue dashed line, resulting in a χ^2/dof $\sim 9 \times 10^{-3}$, where dof is the number of degrees of freedom. The data is also fit to the multilevel expression [square of Eq. (10b)] shown as the red solid line, resulting in χ^2/dof $\sim 8 \times 10^{-4}$. The χ^2 is computed assuming equally weighted data points (uncertainty for each point equal to unity). Final m-level populations, $\Pi_{J_g m_g}$, were estimated from the multilevel fits and are tabulated in Table I. Pulse parameters: detuning $\Delta \sim 50$ MHz, intensity $I \sim 50$ mW/cm^2, polarization state $|q_L| = 1$, first-pulse duration $\tau_1 = 300$ ns.

It is also possible to estimate the final m-level populations, $\Pi_{J_g m_g}$, from the multilevel fits to the data in Fig. 6. Although we found the statistical errors in the populations from the fits to be relatively large, the estimates are considered accurate for two reasons. First, a variation between the $\Pi_{J_g m_g}$ on the order of $\sim$10% results in a deviation in the minimum of the χ^2. Second, the distribution of populations is similar to those inferred from simulations. We attribute the large statistical errors to the presence of 12 free parameters in the fit function [based on the square of Eq. (10a)], namely, u_2, θ, Δt, ω_q, an amplitude factor A, and the seven populations, $\Pi_{J_g m_g}$.

TABLE I. Final m-level population estimates from multilevel fits to experimental data for various second-pulse durations, as shown in Fig. 6. The fits were performed assuming $q_L = 1$.

τ_2 (ns)	Π_{3-3}	Π_{3-2}	Π_{3-1}	Π_{30}	Π_{31}	Π_{32}	Π_{33}
70	0.00	0.03	0.32	0.48	0.15	0.02	0.00
86	0.00	0.03	0.38	0.32	0.21	0.05	0.01
98	0.00	0.00	0.50	0.32	0.15	0.02	0.01

From Table I, the general trend in the final populations is to move toward the $m_g > 0$ levels as the pulse duration increases. This is consistent with our expectations for σ^+ excitation pulses. Magnetic sublevel populations can be confirmed using independent techniques [25].

Figure 7 shows data from the two-pulse recoil experiment obtained using circularly polarized beams and separately for linearly polarized beams. This data provides alternate confirmation of the role of magnetic sublevels. The recoil curves for each polarization state are qualitatively different for various second-pulse durations. This figure also shows simulations that qualitatively agree with the data.

The signal shapes shown in Fig. 7 for each polarization are consistent with our expectations based on two considerations. First, the backscattered field amplitude from each m level is proportional to $(C^{J_g\ 1\ J_e}_{m_g\ q_L\ m_e})^2 \Pi_{J_g m_g}$. For the same distribution of m-level populations at the time of the echo, the two polarizations of the readout pulse induce different atomic responses and therefore produce distinct signal shapes for the two cases. Second, the atom-field couplings are larger toward the $m_g = J_g$ state for the $q_L = 1$ polarization state ($C^{3\ 1\ 4}_{3\ 1\ 4} = 1$) compared to the couplings for the $m_g = 0$ state

($C^{3\ 1\ 4}_{0\ 1\ 1} \sim 0.598$). As a result, in the presence of spontaneous emission, circularly polarized sw pulses produce extreme-state pumping. Similarly, for a linearly polarized sw pulse, the atom-field couplings are largest for the $m_g = 0$ state ($C^{3\ 1\ 4}_{0\ 0\ 0} \sim 0.756$, while $C^{3\ 1\ 4}_{3\ 0\ 3} = 0.5$). Consequently, there is optical pumping toward the $m_g = 0$ state. In this case, however, the atom-field coupling is not as strong as it is for the $m_g = J_g$ state with a σ^+-polarized beam. Therefore, for a given field strength, higher-order momentum states will be populated for circularly polarized excitations. As a result of these two considerations, the recoil curves are qualitatively different for linear and circular polarizations.

Figure 8 shows data overlaid with the prediction of the two-level model [Eq. (6)] as well as output from numerical simulations for the conditions of the experiment. Only a temporal shift and amplitude scaling has been applied to the predictions of the analytical model and the simulation—no fits were performed in this plot. It is clear that the simulation successfully models the data for measured pulse parameters such as the detuning, pulse duration, and intensity. The initial sublevel populations are not measured in the experiment and were assumed to be similar to those measured in Table I (distribution peaked near $m_g = 0$). In contrast, the two-level model gives a poor prediction of the signal shape when the
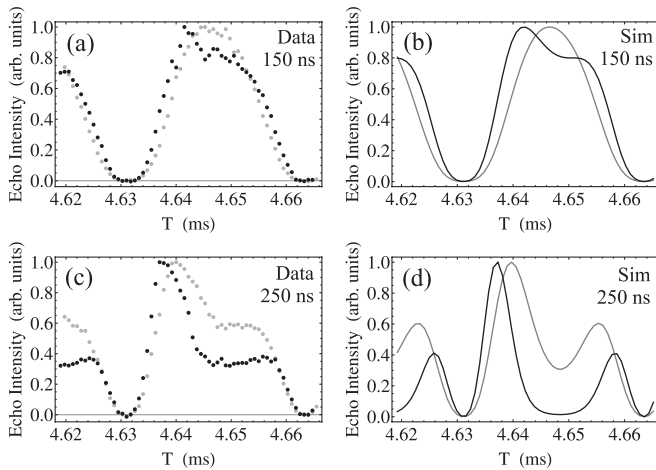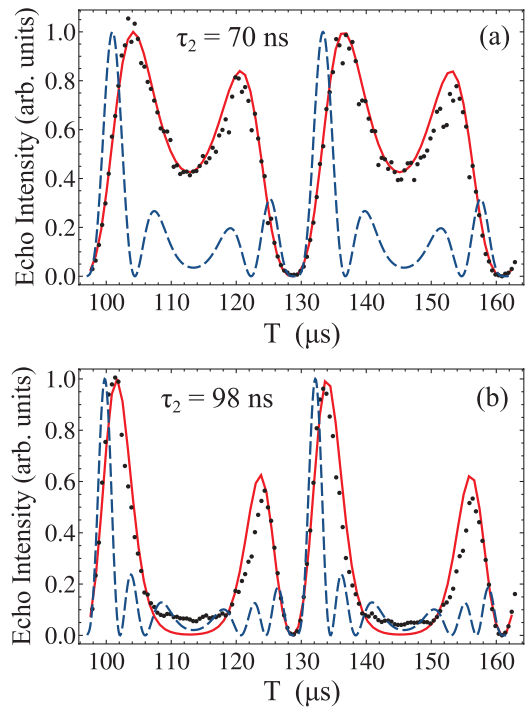

FIG. 7. Data from the two-pulse recoil experiment (a,c) and corresponding simulations (b,d) for two laser polarization states (gray, $q_L = 0$; black, $|q_L| = 1$) and two second-pulse durations (a,c: $\tau_2 = 150$ ns; b,d: $\tau_2 = 250$ ns). The recoil signals are qualitatively different for the two polarizations because of effects due to magnetic sublevels. In the simulation, we used initial m-level populations $\Pi_{J_g m_g}(0) = \{0.05, 0.10, 0.20, 0.30, 0.20, 0.10, 0.05\}$, where $m_g = -3$ on the left and $m_g = 3$ on the right, which produced the best agreement with the data for measured pulse parameters. Pulse parameters: detuning $\Delta \sim 40$ MHz, intensity $I \sim 13$ mW/cm^2, first-pulse duration $\tau_1 = 500$ ns, pulse rise time $\tau_{\rm rise} = 20$ ns.

FIG. 8. (Color online) Data from the two-pulse recoil experiment for second-pulse durations $\tau_2 = 70$ ns (a) and 98 ns (b) overlayed with predictions of the two-level theoretical model [Eq. (6), dashed blue curve] and a multilevel simulation (solid red curve). No fits were performed here. There is good agreement between the simulation and the data for measured pulse parameters. In contrast, the two-level theory gives a poor prediction of the data for the same parameters. The distribution of initial m-level populations in the simulations was set to be similar to those shown Table I: $\Pi_{J_g m_g}(0) = \{0.05, 0.10, 0.25, 0.35, 0.20, 0.03, 0.02\}$. Pulse parameters: $\tau_1 = 300$ ns, $\tau_{\rm rise} = 20$ ns, $\Delta \sim 8.36 \Gamma_{\rm N}$, $\Omega_0 \sim 5.2 \Gamma_{\rm N}$.

measured pulse parameters are used as inputs. These results suggest that the simulation can be used to study a variety of properties associated with this interferometer, including possible systematics that would affect a precision measurement of the recoil frequency. We discuss other applications of the simulation in Sec. VI.

B. Phase evolution during standing-wave interaction

We now describe the phase evolution of momentum states subject to sw excitation. We separate the discussion into three parts: phase dynamics due to spontaneous emission, phase dynamics due to stimulated emission and absorption, and a measurement of the combined effects including magnetic sublevels. These effects are expected to be important for matter-wave interference when the excited state contributes significantly to the relative phase between the different momentum states of the ground level. We describe these effects in the context of a single sw interaction using a theoretical treatment and compare the theoretical predictions to the results of simulations. Finally, we observe trends associated with these effects using the echo AI and verify these observations using two-pulse simulations.

1. Spontaneous emission

In this section, we summarize our theoretical understanding of the influence of spontaneous emission on the shape of the recoil signal. The expression for the one-pulse recoil signal [Eq. (A16)] contains the essential physics relevant for this discussion. The consequences of spontaneous emission on the two-pulse recoil signal [Eq. (6)] stem from the same effects as those in the one-pulse signal.

There are two main features that are observed as a consequence of including spontaneous emission in the theory. First, within a single period, maxima adjacent to the signal zeros have different amplitudes. We refer to this as the asymmetry in the recoil signal. Second, there is a temporal shift of the zeros in the signal toward earlier times relative to the zeros without spontaneous emission. Both of these features are best demonstrated when the pulse area is large—causing the double-peak structure within each period of the recoil signal. This is illustrated in Fig. 9 on the basis of Eq. (A16) and has been observed experimentally (see Figs. 6, 7, and 8). Both of these features are present only when the spontaneous emission parameter, θ, is nonzero [see Eq. (3)].

For the moment we consider a system without spontaneous emission ($\theta = 0$ and the complex pulse area, $\Theta_1 \equiv u_1 e^{i\theta}$, is real). The signal develops multiple peaks within each period for large pulse areas [compare Fig. 3(c) to Fig. 3(d)]. This structure is due to the interference of higher-order momentum states which become more populated as u_1 increases. We demonstrate this interference by truncating the infinite sum in Eq. (A11) to only $n = -2, \ldots, 2$ so that

$$
\begin{aligned}
i\tilde{E}_1(t) \approx &-J_2(\Theta_1)J_1(\Theta_1^*)e^{-i3\omega_q t} - J_1(\Theta_1)J_0(\Theta_1^*)e^{-i\omega_q t} \\
&+ J_0(\Theta_1)J_1(\Theta_1^*)e^{i\omega_q t} + J_1(\Theta_1)J_2(\Theta_1^*)e^{i3\omega_q t} \\
&+ J_2(\Theta_1)J_3(\Theta_1^*)e^{i5\omega_q t}.
\end{aligned}
\tag{21}
$$

This expression contains the first three harmonics of the backscattered electric field that oscillate with frequencies $\pm\omega_q$,
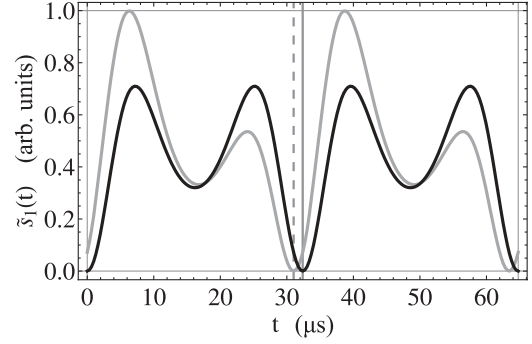

FIG. 9. Comparison of recoil curves (backscattered field intensity as a function of time) predicted by the one-pulse theory [Eq. (A16)], with and without spontaneous emission. The black curve corresponds to a spontaneous emission-free system ($\Gamma = 0 \to \theta = 0$), while the gray curve corresponds to a system where spontaneous emission is present ($\Gamma = \Gamma_N \to \theta = -0.133$ rad). The solid vertical grid line shows the first zero in the signal after $t = 0$ in the absence of spontaneous emission, while the dashed grid line shows the zeros shift by a temporal amount $\delta t = \theta/\omega_q$ in the presence of spontaneous emission. Pulse parameters: $\Delta = 7.5\Gamma_N$, $\Omega_0 = 1.5\Gamma_N$, $\tau_1 = 250$ ns, pulse area $u_1 \sim 1.43$.

$\pm 3\omega_q$, and $5\omega_q$, respectively. The sum of different harmonics gives rise to constructive and destructive interference in the field amplitude. The result is a diminished amplitude between the zero crossings of the total backscattered field—producing the double-peaked structure. This effect is shown in Fig. 10 using the terms corresponding to $n = 0$, 1, and 2 in Eq. (21). In the absence of any phase shifts of the individual harmonics, the shape of the recoil signal [$\tilde{s}_1(t) = |\tilde{E}_1(t)|^2$] is symmetric (black curve in Fig. 9).

We now consider the case where spontaneous emission is present in the system ($\theta \neq 0$). The spontaneous emission parameter, θ, causes a phase shift of each harmonic comprising $\tilde{E}_1(t)$ in Eq. (2). This is demonstrated by expanding the Bessel functions in Eq. (21) in a Taylor series and keeping only the leading terms:

$$
\begin{aligned}
\tilde{E}_1(t) \approx &-\left(u_1 + \frac{u_1^5}{32}\right)\sin(\omega_q t - \theta) + \frac{u_1^3}{4}\sin(\omega_q t + \theta) \\
&+ \frac{u_1^3}{8}\sin(\omega_q t - 3\theta) - \frac{u_1^3}{8}\sin(3\omega_q t - \theta) \\
&+ \frac{u_1^5}{64}\sin(3\omega_q t + \theta) + \frac{u_1^5}{96}\sin(3\omega_q t - 3\theta).
\end{aligned}
\tag{22}
$$

Each term in Eq. (22) has been phase shifted by an integer multiple of θ, but no two terms are shifted by the same temporal amount [colored curves in Fig. 10(b)]. When all values of n are included, the different temporal shifts sum to a net shift of $\delta t = \theta/\omega_q$ [shown by the dashed grid lines in Figs. 9 and 10(b)].

Figure 10(b) illustrates the harmonic components of the backscattered field amplitude [$\tilde{E}_1(t)$ from Eq. (2)] associated with the interference $\langle n\hbar q | (n+1)\hbar q \rangle$ for $n = 0$, 1, and 2 using $\theta = -0.133$ rad. When summed over all harmonics, the field exhibits more constructive interference on one side of the wave form than the other [black curve in Fig. 10(b)], giving rise to an asymmetry in the peak amplitude within each recoil period and a temporal shift of the zeros. The corresponding field intensity,
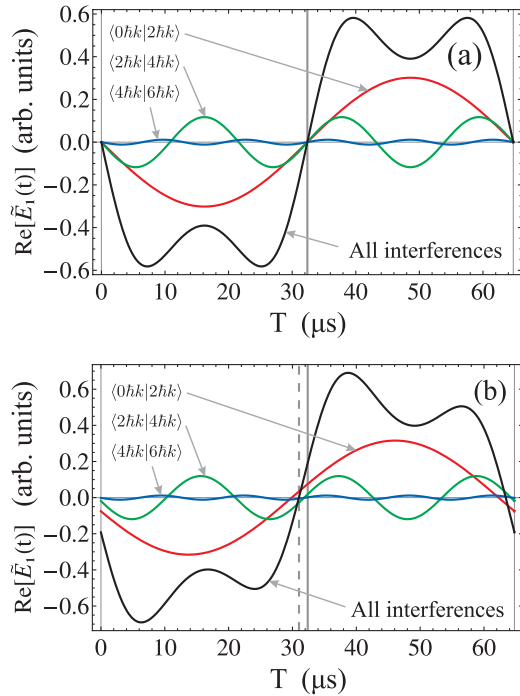
FIG. 10. (Color online) Real part of the harmonics comprising the backscattered electric field, $\tilde{E}_1(t)$ [Eq. (A11)], for a system without spontaneous emission (a, $\theta = 0$) and with spontaneous emission (b, $\theta = -0.133$ rad). Each graph shows harmonics associated with the interference of momentum states $|n\hbar q\rangle$ and $|(n+1)\hbar q\rangle$ for $n = 0$, 1, and 2 (red, green, and blue curves, respectively). These harmonics correspond to the $n = 0$, 1, and 2 terms in Eq. (A11). The total backscattered field, shown as the black curve, is the sum of all harmonics due to the interference between p states differing by $\hbar q$. In (b), the total scattered field is shifted by a temporal amount $\delta t = \theta / \omega_q$ as shown by the dashed grid line. Note that the imaginary part of $\tilde{E}_1(t)$ sums to zero in both (a) and (b) when all terms in Eq. (A11) are included. The pulse parameters are the same as in Fig. 9.

$\tilde{s}_1(t)$, is shown in Fig. 9 as the gray curve. When $\theta = 0$, there is no temporal shift, thus no asymmetry, and we recover the black curve in Fig. 9.

In the experiment, we always observe a negative asymmetry, which means that the amplitude of the first peak of the recoil signal is higher than the second peak between consecutive zeros, as shown in Figs. 6 and 8. A positive asymmetry corresponds to the second peak amplitude being larger than the first. A negative asymmetry implies that the zeros of the signal are shifted toward earlier times ($\theta, \delta t < 0$), which is a consequence of using a positive detuning. These observations are consistent with theoretical predictions.

The phases of each harmonic in Eq. (22) represent the difference in phase between two interfering momentum states. This phase difference is a direct result of the decay of the excited state into the ground state. When the harmonics are summed over, the relative phases are effectively averaged and the resulting phase shift of the scattered field amplitude represents a weighted average phase difference between all interfering momentum states that differ by $\hbar q$. To first order, this phase is approximately equal to θ. Spontaneous emission is evidently one mechanism by which the relative phases of two interfering momentum states can be nonzero. In the

next section, we show that stimulated emission and absorption produce similar effects.

2. Stimulated emission and absorption

In this section, we illustrate that stimulated emission and absorption between the ground and excited levels leads to a time-dependent asymmetry in the recoil signal. To isolate this effect, we generate simulations of the one-pulse recoil signal in the absence of spontaneous emission (i.e., $\Gamma = 0$). Under these conditions, the signal exhibits either positive or negative asymmetry depending on the pulse duration, τ_1, as shown in Fig. 11. This originates from the dynamic evolution of the atomic state amplitudes during the sw pulse (Rabi oscillations) due to stimulated emission and absorption. In contrast, the analytical theory for the one-pulse recoil signal [Eq. (A16)], which ignores the dynamic exchange of population between the ground and excited states [see Eq. (A2a)], predicts that there should be no asymmetry or phase shift when there is no spontaneous emission. Results from the simulations indicate that, by changing τ_1, the asymmetry oscillates between positive and negative at the same frequency as the generalized Rabi frequency.

The oscillations in the asymmetry shown in Fig. 11 originate from the time-dependence of the relative phase between interfering momentum states. As the interaction time with the sw pulse increases, there is a transfer of momentum from the ground state to the excited state and back to the ground state again. The intermediate process of going through the excited state imprints a momentum-dependent phase on the ground-state wave function. As a result, the phase difference between two adjacent p states changes as a function of the interaction time, τ_1.
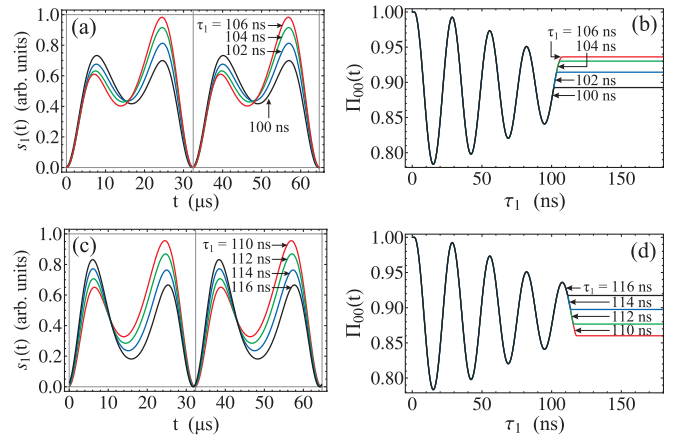

FIG. 11. (Color online) Simulations of one-pulse recoil signal, $s_1(t)$, in the absence of spontaneous emission for pulse durations varying within one Rabi oscillation ($\tau_1 \sim 100$–116 ns). In (a) the recoil signal begins roughly symmetric at $\tau_1 = 100$ ns. As τ_1 is increased, the signal exhibits positive asymmetry and shifts toward later times. Panel (b) shows the corresponding Rabi oscillation in the ground-state population for each τ_1 in (a). In (c) the signal shifts toward earlier times and shows negative asymmetry as τ_1 increases from 110 to 116 ns. Panel (d) shows the corresponding Rabi oscillations for (c). Here the generalized Rabi frequency is $\sqrt{\Omega_0^2 + \Delta^2} \sim 5.4\Gamma_N \sim 32$ MHz. Pulse parameters: $\tau_{rise} \sim 1$ ns, $\Delta = 5\Gamma_N$, $\Omega_0 = 2\Gamma_N$, $\Gamma = 0$.

The amplitude of the phase oscillation is largely dependent on the bandwidth of the sw pulse, which has contributions from the pulse duration, τ_1, and the rise time, $\tau_{\rm rise}$. A large-bandwidth pulse produces a large-amplitude phase oscillation. As τ_1 increases, the bandwidth of the pulse decreases—giving rise to a damping of the oscillation amplitude. This result can also be inferred from the time-dependence of the excited-state population, since the relative phase between momentum states is a measure of its contribution to the recoil signal.

3. Combined phase effects

In the experiment, both stimulated and spontaneous processes contribute to phase shifts of the recoil signal. In the following section, we discuss the combination of these two mechanisms and measure their affect on the signal. This constitutes one of the most important results in this article.

We first describe an analytical calculation that predicts a dynamic phase for each momentum state that depends on both the parameter θ [Eq. (3)], which is a measure of the number of spontaneous emission events, and the pulse area u_1, which is a measure of the number of stimulated processes. This calculation is valid for the one-pulse recoil signal.

Since the interferometer is sensitive to the relative phase of interfering momentum states, this p-dependent phase provides a direct connection between matter-wave interference and transitions due to both spontaneous and stimulated processes. However, the calculation of the relative phase is subject to the limitations of the theoretical framework developed in Sec. III (weak, far off-resonance pulses and short interaction times). This necessitates the use of simulations to develop more accurate predictions.

When spontaneous emission is included in the theory, the excited state imprints a momentum-dependent phase, $\phi(p)$, on the ground-state wave function, which can be obtained from

$$\phi(p) = \arg[a_g(p)], \tag{23}$$

where $a_g(p)$ is the amplitude of state $|p\rangle$ in the ground level. The phase of a discrete momentum state $|p = n\hbar q\rangle$ can be obtained using Eq. (A7) for $a_g(p)$:

$$\phi_n^{(1)} = \arg[(-i)^n J_n(u_1 e^{i\theta})], \tag{24}$$

where the superscript (1) indicates that this calculation is valid for a single sw pulse and the subscript n labels the momentum state. Expanding the Bessel function in a series in powers of $u_1 e^{i\theta}$, one can show that

$$
\tan\left(\phi_n^{(1)} + n\frac{\pi}{2}\right)
$$
$$
= \frac{\sum_{j=0}^{\infty} \frac{(-1)^j}{j!(j+|n|)!} \left(\frac{u_1}{2}\right)^{2j+|n|} \sin[(2j+|n|)\theta]}{\sum_{l=0}^{\infty} \frac{(-1)^l}{l!(l+|n|)!} \left(\frac{u_1}{2}\right)^{2l+|n|} \cos[(2l+|n|)\theta]}. \tag{25}
$$

To first order: $\phi_n^{(1)} \approx |n|\theta - n\pi/2$, which is independent of the pulse area, u_1, and therefore ignores stimulated processes. This

result indicates that the phase difference between interfering momentum states is

$$\Delta\phi_n^{(1)} = \phi_n^{(1)} - \phi_{n-1}^{(1)} \approx \begin{cases} \theta + \pi/2 & \text{for} \quad n \geqslant 1, \\ -\theta + \pi/2 & \text{for} \quad n < 1. \end{cases} \tag{26}$$

For higher orders, however, stimulated processes contribute to the phase of each momentum state and there is a distinct dependence on the pulse area. The AI is sensitive to the average relative phase between p states that differ by $\hbar q$. For an arbitrary ground state amplitude $a_g(p)$, this quantity can be expressed as

$$\langle\Delta\phi\rangle = \arg\left[\int a_g(p)a_g^*(p-\hbar q)\,dp\right], \tag{27}$$

where the $\langle\cdots\rangle$ notation denotes an average over momentum. For the specific case of the one-pulse recoil experiment, the average relative phase is

$$\langle\Delta\phi^{(1)}\rangle = \arg\left[-i\sum_n J_n(u_1 e^{i\theta})J_{n-1}(u_1 e^{-i\theta})\right], \tag{28}$$

which has a distinct dependence on the sw pulse duration, τ_1.

Figure 12 illustrates the dependence of $\langle\Delta\phi^{(1)}\rangle$ on the sw pulse duration, τ_1. Predictions are shown for both theory [dashed red line—Eq. (28)] and simulations in the presence and absence of spontaneous emission [dotted blue and solid black lines, respectively—Eq. (27)].

For small τ_1, the theoretical expression for the average relative phase [Eq. (28)] is approximately equal to θ. This result can also be inferred from Eq. (26), which is valid only for small u_1. According to theory, the contribution from spontaneous emission is a constant phase offset equal to θ [Eq. (3)]. As the interaction time increases, the theory predicts an increase in $|\langle\Delta\phi^{(1)}\rangle|$, as well as a slow oscillation. The frequency of this oscillation is empirically determined to be
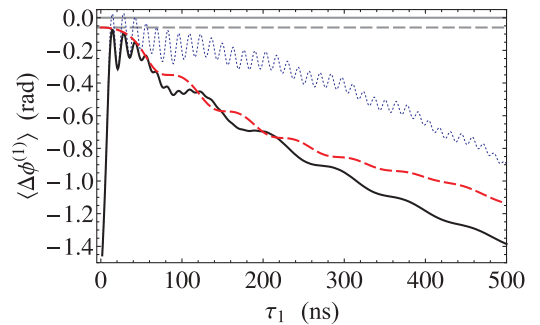

FIG. 12. (Color online) Average relative phase between momentum states differing by $\hbar q$ as a function of sw pulse duration, τ_1. An offset of $\pi/2$ has been added to the vertical axis. The dashed gray horizontal grid line shows the value of $\theta \sim -0.06$ rad from Eq. (3). The dashed red line is a calculation based on Eq. (28) with u_1 given by Eq. (A4). The dotted blue line shows the prediction of Eq. (27) computed from a simulation in the absence of spontaneous emission. The solid black line is the analogous prediction of a simulation including spontaneous emission. The steep rise of the two simulations at small τ_1 represents the first Rabi cycle of phase transfer from $p = 0$ to neighboring states. These states initially have zero amplitude and their phases are not well defined. Pulse parameters: $\tau_{\rm rise} \sim 1$ ns, $\Delta = 8.4\Gamma_{\rm N}$, $\Omega_0 = 4.5\Gamma_{\rm N}$.

$\sim 2\Omega_0^2/\Delta \sim 2.7$ MHz, which is due to stimulated emission and absorption.

Results of simulations in the absence of spontaneous emission (dotted blue line) show an additional high-frequency oscillation in $\langle\Delta\phi^{(1)}\rangle$ as a function of τ_1. These oscillations are caused by the transfer of phase between the ground and excited state due to stimulated processes and have a frequency approximately equal to the generalized Rabi frequency $\sqrt{\Omega_0^2 + \Delta^2} \sim 56$ MHz. These high-frequency phase oscillations are not taken into account in Eq. (28) as a result of the far off-resonance assumption. When spontaneous emission is included in the simulations (solid black line), the oscillations are highly damped. As the pulse area increases, there is a significant departure of the theory from the simulations. We attribute this departure to the absence of dynamic population transfer between the ground and excited states and the weak-field assumption made in the theory.

We now review results of measurements of the average relative phase, $\langle\Delta\phi^{(2)}\rangle$, from the two-pulse recoil experiment and corresponding simulations. Figure 13 shows the variation in $\langle\Delta\phi^{(2)}\rangle$ as a function of τ_2. This variation corresponds to the change in the asymmetry of the signal shapes shown in Fig. 6. We measure $\langle\Delta\phi^{(2)}\rangle$ from the data by fitting to the square of Eq. (10b) (which includes effects due to m levels) and using the best-fit value of θ. From the data, $\langle\Delta\phi^{(2)}\rangle$ seems to decrease and level out near -35 mrad after $\tau_2 \sim 90$ ns. This can be explained by the excited-state population approaching steady state—giving rise to a saturation of momentum-state excitation.

Figure 13 also shows results of two-level simulations ($J_g = 0$) implemented with the same pulse parameters as the
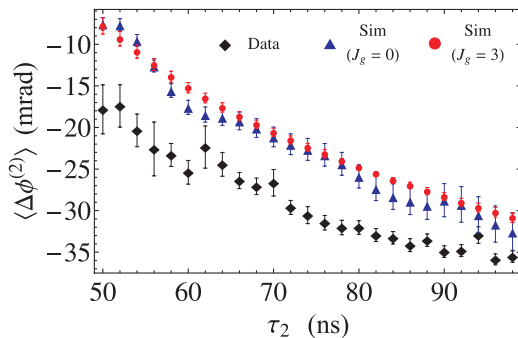

FIG. 13. (Color online) Variation of average relative phase, $\langle\Delta\phi^{(2)}\rangle$, as a function of second-pulse length. The relative phase measured from fits to experimental data (diamonds) are overlayed with the results of a two-level simulation (triangles, where $J_g = 0$) and a multilevel simulation (circles, where $J_g = 3$). A subset of the multilevel simulations overlayed with data is shown in Fig. 8. $\langle\Delta\phi^{(2)}\rangle$ is measured from the data and the multilevel simulation by fitting to the square of Eq. (10b) and using the best-fit value of θ. Similarly, it is measured for the two-level simulation by fitting to Eq. (6). A subset of the data from which $\langle\Delta\phi^{(2)}\rangle$ is extracted is shown in Fig. 6, with the corresponding fits shown as solid red curves. The error bars for each set of points are equal to the statistical uncertainties in θ from the corresponding fits. The pulse parameters are the same as those in Fig. 6, except for the two-level simulations where the rise time was reduced to $\tau_{\rm rise} = 10$ ns to illustrate the presence of oscillations in $\langle\Delta\phi^{(2)}\rangle$ as a function of τ_2.

data (except for the rise time which was set to $\tau_{\rm rise} = 10$ ns). Here, $\langle\Delta\phi^{(2)}\rangle$ is measured by fitting each recoil curve generated by the simulation to Eq. (6) (which incorporates only two levels). This is equivalent to the method used to measure the average relative phase from data. The trend of the two-level simulation is qualitatively similar to the black curve shown in Fig. 12. In comparison to the data, we find an additional superimposed oscillation and a constant phase offset. The frequency of this phase oscillation is the same as the generalized Rabi frequency ($\sqrt{\Omega_0^2 + \Delta^2} \sim 59$ MHz in this case). This is consistent with effects due to stimulated emission and absorption, as discussed in Sec. V B 2. The oscillations are quickly damped as the excited state population approaches steady state. The rate at which this occurs is mainly determined by the bandwidth of the pulse (which has contributions from both τ_2 and $\tau_{\rm rise}$) and the spontaneous emission rate. In these two-level simulations, we have reduced the rise time of the sw pulses from 20 ns (as measured in the experiment) to 10 ns in order to demonstrate the presence of these oscillations.

The red circles shown in Fig. 13 represent simulations including magnetic sublevels ($J_g = 3$). These results show no phase oscillations as a function of interaction time, which is consistent with the data. The absence of phase oscillations in the data and the multi-level simulation is attributed to the relatively long rise time ($\tau_{\rm rise} \sim 20$ ns) of the excitation pulses, as discussed in the previous subsection. There is also additional damping of phase oscillations due to the interference between backscattered fields from each ground-state magnetic sublevel.

Although the trend in $\langle\Delta\phi^{(2)}\rangle$ from both the two-level and the multilevel simulations is similar to the data, there is a small phase offset between the two. This can be explained in the following manner. First, the offset is equivalent to a difference in the level of asymmetry between the data and the simulations. This is not surprising since our estimates of various input parameters, such as the Rabi frequency and m-level populations, are not directly measured in the experiment. Second, our ability to measure $\langle\Delta\phi^{(2)}\rangle$ from the data is limited by the signal-to-noise. Since $\langle\Delta\phi^{(2)}\rangle$ is estimated by fitting to the data, and each point in the fit is equally weighted, this results in an overestimation of the phase value and an underestimation in the uncertainty of that value. This is especially true at small τ_2. This is because the quantity being measured is highly shape-dependent and, at small τ_2, where there is very little asymmetry in the data, a small amount of noise can cause a large error in the measurement.

The time evolution of the relative phase predicted by the two-level and the multilevel simulations, however, are very similar. This suggests that $\langle\Delta\phi^{(2)}\rangle$ is largely unaffected by the presence of magnetic sublevels but depends mostly on the sw pulse parameters and the magnitude of the spontaneous emission rate—which, aside from the pulse rise time, were the same in both simulations. This is consistent with the theory presented earlier.

In a previous article [16], we investigated the influence of spontaneous emission on the two-pulse recoil signal using both theory and experiments. We used a phenomenological model for the two-pulse recoil signal that was successful in predicting the asymmetry in the signal shape and the temporal offset. Since the spontaneous emission parameter, θ, is related to the spontaneous emission rate, Γ, it appeared that there was

a variation in Γ with the pulse duration and a measurement of Γ appeared to be possible by fitting experimental data using this model (Eq. (26) in Ref. [16]). However, the average relative phase of the signal, $\langle\Delta\phi^{(2)}\rangle$, depends on both θ and the pulse area. The phenomenological model did not take into account this pulse-area dependence. As a result, erroneous values of θ, and therefore Γ, were measured when τ_2 changed. Thus, the conclusion that Γ depended on τ_2 was not justified. The dependence of the average relative phase on spontaneous and stimulated processes, as well as effects due to magnetic sublevels, was not fully understood until recently. With this interpretation, we can explain the variation of θ with τ_2 observed in Ref. [16].

VI. CONCLUSION

We have developed a comprehensive numerical simulation of a time-domain echo interferometer that is successful in predicting a variety of physical effects associated with matter-wave interference. The simulation accurately models experimental results for measured input parameters. Based on these results, we have determined that the interference between backscattered electric fields from each ground-state magnetic sublevel significantly affects the signal shape, which is consistent with experimental observations. Additionally, a more complete understanding of the phase modulation of the atomic wave function induced by sw pulses has been developed on the basis of the simulation.

The simulation motivated the development of an improved analytical model of the signal that accounts for both spontaneous emission and ground-state magnetic sublevels. Using the analytical model, we were able to improve the relative error in measurements of the recoil frequency by a factor of ~ 3. We were also able to estimate magnetic sublevel populations at the time of the readout pulse.

Through theoretical analysis and simulations, we have clarified the role of spontaneous emission on the recoil signal. We have also explained how the relative phase between interfering momentum states affects the signal on the basis of stimulated emission and absorption, which is most important when the excited state is significantly populated. These effects are not unique to the AI considered in this article, but apply more generally to interferometers that involve momentum-state interference induced by laser excitation, such as frequency-domain AIs [26].

The robustness of the simulations suggest that they can be used to study the AI under a variety of interesting conditions, such as the near-resonance ($|\Delta| \sim \Gamma$), high-intensity ($\Omega_0 \sim |\Delta|$), or long-pulse ($\tau_j \gg |\Delta|^{-1}$) regimes. An important application of this work also includes the study of systematic effects on a precision measurement of the atomic recoil frequency using the three-pulse technique outlined in Refs. [13,16].

APPENDIX

We review the calculation of the recoil signal in the one-pulse regime. The evolution of the atomic state amplitudes is governed by the Schrödinger equation

$$\tilde{\mathcal{H}} \begin{pmatrix} a_e \\ a_g \end{pmatrix} = i\hbar \begin{pmatrix} \dot{a}_e \\ \dot{a}_g \end{pmatrix}, \tag{A1}$$

where $\tilde{\mathcal{H}}$ is the Hamiltonian given by Eq. (1). We assume that the rate of change of the excited state amplitude is small compared to the detuning ($|\dot{a}_e| \ll |\Delta|$), which results in the following relations:

$$a_e = \frac{\Omega e^{i\theta}}{(\Delta^2 + \gamma^2)^{1/2}} a_g, \tag{A2a}$$

$$\dot{a}_g = -i \frac{\Omega^2 e^{i\theta}}{(\Delta^2 + \gamma^2)^{1/2}} a_g. \tag{A2b}$$

Here θ is a phase that characterizes the amount of spontaneous emission occurring during the pulse and is given by Eq. (3). Equation (A2b) is integrated to obtain the ground-state amplitude for a pulse of duration τ_1,

$$a_g(\boldsymbol{r}) = a_g(\boldsymbol{r},0)e^{-i\Theta_1 \cos q \cdot r}, \tag{A3}$$

where $\boldsymbol{q} = \boldsymbol{k}_1 - \boldsymbol{k}_2 = 2\boldsymbol{k}$ is the difference between the k vectors comprising the sw and $\Theta_1 \equiv u_1 e^{i\theta}$ is the complex pulse area with magnitude u_1 given by

$$u_1 \equiv \frac{\Omega_0^2 \tau_1}{2\Delta} \left[1 + \left(\frac{\Gamma}{2\Delta} \right)^2 \right]^{-1/2}. \tag{A4}$$

We assume the initial state of the atom to be a plane wave, $a_g(\boldsymbol{r},0) = V^{-1/2} e^{ip_0 \cdot r/\hbar}$, with momentum $\boldsymbol{p}_0 = M\boldsymbol{v}_0 = \hbar\boldsymbol{k}_0$ and interaction volume V.

In Eq. (A3) we have ignored a $-i\Theta_1$ term in the exponent because it is independent of $\boldsymbol{r}$ and is therefore unimportant for interference. It also causes a_g to decay exponentially during the pulse (since Θ_1 is a complex quantity), which does not preserve normalization. Since we assume the system is closed (no atoms are being lost), this corresponds to an unwanted physical process and is a direct result of using a Hamiltonian that is non-Hermitian [Eq. (1)].

From Eq. (A3), it is clear that the effect of interacting with the sw pulse is to spatially modulate the phase of the ground-state amplitude. Equivalently, the sw field is a phase grating that diffracts the atomic wave function into a superposition of momentum states. Using the Jacobi-Anger expansion, we decompose the ground-state amplitude into its harmonics,

$$a_g(\boldsymbol{r}) = a_g(\boldsymbol{r},0) \sum_{n=-\infty}^{\infty} (-i)^n J_n(\Theta_1) e^{inq \cdot r}, \tag{A5}$$

where $J_n(x)$ is the nth-order Bessel function of the first kind. Here, the index n indicates the order of each harmonic, which corresponds to a specific momentum state: $e^{inq \cdot r} \propto$

$|\boldsymbol{p} = n\hbar\boldsymbol{q}\rangle$. The sw pulse only populates the ground state with even multiples of the photon momentum, $\hbar\boldsymbol{k}$. In contrast, the excited state is populated with only odd multiples of $\hbar\boldsymbol{k}$ due to an extra factor of $\Omega(\boldsymbol{r})$ in the excited-state amplitude, a_e, which can be written as

$$a_e(\boldsymbol{r}) = \frac{\Omega_0 e^{i\theta}}{2(\Delta^2 + \Gamma^2)^{1/2}} a_g(\boldsymbol{r},0)$$
$$\times \sum_n (-i)^n J_n(\Theta_1)[e^{i(2n-1)k\cdot r} + e^{i(2n+1)k\cdot r}]. \quad \text{(A6)}$$

The population of each momentum state, $|J_n(\Theta_1)|^2$, is completely determined by the magnitude of the pulse area, u_1. However, the phase of each momentum state is determined by both the magnitude *and* the phase of the pulse area, u_1 and θ, respectively. This has an important consequence for the interference of two momentum states (see Sec. V B 3).

After the sw pulse turns off, the atom evolves in free space. The population of the excited state is scaled by a factor $\Omega_0/|\Delta| \ll 1$ compared to the ground state and is therefore ignored. The Hamiltonian in free space contains only the kinetic energy term, $\hat{P}^2/2M$, where $\hat{P}$ is the momentum operator. Therefore, the calculation of the ground-state amplitude at time t is much more transparent by transforming into momentum space:

$$a_g(\boldsymbol{p}) = \frac{(2\pi\hbar)^{3/2}}{\sqrt{V}} \sum_n (-i)^n J_n(\Theta_1)\delta^3(\boldsymbol{p} - \boldsymbol{p}_0 - n\hbar\boldsymbol{q}). \quad \text{(A7)}$$

The solution to the Schrödinger equation in this regime dictates that the phase of the ground-state amplitude is modulated differently for each momentum state:

$$a_g(\boldsymbol{p},t) = a_g(\boldsymbol{p}) \exp\left[-\frac{i}{\hbar}\frac{p^2}{2M}t\right]. \quad \text{(A8)}$$

By transforming back to position space, the ground-state amplitude *a* time t after the sw pulse is

$$a_g(\boldsymbol{r},t) = \frac{1}{\sqrt{V}} e^{i(p_0\cdot r - \epsilon_0 t)/\hbar}$$
$$\times \sum_n (-i)^n J_n(\Theta_1) e^{inq\cdot r} e^{-inq\cdot v_0 t} e^{-in^2\omega_q t}, \quad \text{(A9)}$$

where $\epsilon_0 = p_0^2/2M$ is the initial kinetic energy of the atom, $\boldsymbol{v}_0 = \boldsymbol{p}_0/M$ is the initial velocity, and $\omega_q = \hbar q^2/2M$ is the two-photon recoil frequency.

We are interested in how the ground-state atomic density distribution, $\rho_g(\boldsymbol{r},t) = |a_g(\boldsymbol{r},t)|^2$, evolves in time:

$$\rho_g(\boldsymbol{r},t) = \frac{1}{V} \sum_{n,\eta} i^\eta J_n(\Theta_1) J_{n+\eta}(\Theta_1^*) e^{-i\eta q\cdot r} e^{i\eta q\cdot v_0 t} e^{i\eta(2n+\eta)\omega_q t}. \quad \text{(A10)}$$

This quantity contains a sum over all orders of interference between momentum states and is shown in Figs. 3(a) and 3(b). The index η—equal to the difference between momentum states in multiples of $\hbar\boldsymbol{q}$—denotes the order of the interference. This form of ρ_g helps identify the phase due to spontaneous emission and its subsequent role in the one-pulse recoil signal. The density is modulated in time at integer multiples of ω_q. This multiple depends on the order of the momentum state, n, and the order of the interference, η. The Doppler phase

$\eta\boldsymbol{q}\cdot\boldsymbol{v}_0 t$ results in a dephasing of the density modulation when the density is averaged over the velocity distribution of the atomic sample. However, for the purposes of this discussion, we have assumed that the velocity distribution is infinitely narrow such that Doppler dephasing is negligible. As a result, we have ignored the Doppler phase in all expressions that follow.

The density modulation can be detected in an experiment by measuring coherent Bragg scattering from a traveling wave readout pulse. However, this technique is sensitive only to the q Fourier harmonic of the density distribution when the read-out pulse has the same wavelength, λ, as the sw pulse. This is because Bragg scattering occurs for structures with a spatial periodicity of $m\lambda/2$, for $m = 1, 2, \ldots$. Higher-order spatial harmonics of the density grating (i.e., those periodic at $\lambda/4$, $\lambda/6$, $\ldots$) do not scatter the light. Thus, the backscattered electric-field amplitude is proportional to the q Fourier harmonic of $\rho_g(\boldsymbol{r},t)$, which corresponds to the amplitude of the $e^{-i\eta q\cdot r}$ term in Eq. (A10) with η set to unity:

$$\tilde{E}_1(t) \propto \sum_{n=-\infty}^{\infty} i J_n(\Theta_1) J_{n+1}(\Theta_1^*) e^{i(2n+1)\omega_q t}. \quad \text{(A11)}$$

A simpler form of the backscattered electric field amplitude is realized by using the Bessel function summation theorem [16,18,27]

$$\sum_n J_n(\Theta_1) J_{n+\eta}(\Theta_1^*) e^{i(2n+\eta)\omega_q t} = i^\eta J_\eta(\kappa_1) \left(\frac{\sin(\omega_q t - \theta)}{\sin(\omega_q t + \theta)}\right)^{\eta/2}, \quad \text{(A12)}$$

where

$$\kappa_1 \equiv 2u_1\sqrt{\sin(\omega_q t + \theta)\sin(\omega_q t - \theta)}, \quad \text{(A13)}$$

resulting in the following expression for $\tilde{E}_1(t)$:

$$\tilde{E}_1(t) \propto -J_1(\kappa_1) \left(\frac{\sin(\omega_q t - \theta)}{\sin(\omega_q t + \theta)}\right)^{1/2}. \quad \text{(A14)}$$

However, this form contains a singularity at $t = -(\theta + m\pi)/\omega_q$, which is not physical. The singularity can be removed by using the recurrence relation $2\nu J_\nu(x) = x[J_{\nu-1}(x) + J_{\nu+1}(x)]$, such that

$$\tilde{E}_1(t) \propto -u_1 \sin(\omega_q t - \theta)[J_0(\kappa_1) + J_2(\kappa_1)]. \quad \text{(A15)}$$

The analytical expression for the one-pulse recoil signal, denoted by $\tilde{s}_1$, is the intensity of the backscattered field, which is proportional to $|\tilde{E}_1(t)|^2$:

$$\tilde{s}_1(t) \propto u_1^2 \sin^2(\omega_q t - \theta)[J_0(\kappa_1) + J_2(\kappa_1)]^2. \quad \text{(A16)}$$

This expression for the recoil signal is valid for an atomic sample with a narrow velocity distribution (BEC conditions) after interacting with a single sw pulse.

[1] D. S. Weiss, B. C. Young, and S. Chu, Phys. Rev. Lett. **70**, 2706 (1993).

[2] A. Wicht, J. M. Hensley, E. Sarajlic, and S. Chu, Phys. Scr. T **102**, 82 (2002).

[3] S. W. Chiow, S. Herrmann, S. Chu, and H. Müller, Phys. Rev. Lett. **103**, 050402 (2009).

[4] S. B. Cahn, A. Kumarakrishnan, U. Shim, T. Sleator, P. R. Berman, and B. Dubetsky, Phys. Rev. Lett. **79**, 784 (1997).

[5] E. W. Hagley *et al.*, Phys. Rev. Lett. **83**, 3112 (1999).

[6] S. Gupta, K. Dieckmann, Z. Hadzibabic, and D. E. Pritchard, Phys. Rev. Lett. **89**, 140401 (2002).

[7] M. Cadoret, E. de Mirandes, P. Cladé, S. Guellati-Khélifa, C. Schwob, F. Nez, L. Julien, and F. Biraben, Phys. Rev. Lett. **101**, 230801 (2008).

[8] A. Peters, K. Y. Chung, and S. Chu, Nature (London) **400**, 849 (1999).

[9] B. Dubetsky and M. A. Kasevich, Phys. Rev. A **74**, 023615 (2006).

[10] J. M. McGuirk, G. T. Foster, J. B. Fixler, M. J. Snadden, and M. A. Kasevich, Phys. Rev. A **65**, 033608 (2002).

[11] G. Lamporesi, A. Bertoldi, L. Cacciapuoti, M. Prevedelli, and G. M. Tino, Phys. Rev. Lett. **100**, 050801 (2008).

[12] H. Müller, A. Peters, and S. Chu, Nature (London) **463**, 926 (2010).

[13] S. Beattie, B. Barrett, I. Chan, C. Mok, I. Yavin, and A. Kumarakrishnan, Phys. Rev. A **79**, 021605(R) (2009).

[14] D. V. Strekalov, A. Turlapov, A. Kumarakrishnan, and T. Sleator, Phys. Rev. A **66**, 023601 (2002).

[15] S. Beattie, B. Barrett, I. Chan, C. Mok, I. Yavin, and A. Kumarakrishnan, Phys. Rev. A **80**, 013618 (2009).

[16] S. Beattie, B. Barrett, M. Weel, I. Chan, C. Mok, S. B. Cahn, and A. Kumarakrishnan, Phys. Rev. A **77**, 013610 (2008).

[17] A. Tonyushkin, S. Wu, and M. Prentiss, Phys. Rev. A **79**, 051402(R) (2009).

[18] M. Weel, I. Chan, S. Beattie, A. Kumarakrishnan, D. Gosset, and I. Yavin, Phys. Rev. A **73**, 063624 (2006).

[19] P. R. Berman and V. S. Malinovsky, *Principles of Laser Spectroscopy and Quantum Optics* (Princeton University Press, Princeton, 2010) (preliminary version).

[20] B. Dubetsky and P. R. Berman, Phys. Rev. A **59**, 2269 (1999).

[21] K. Mølmer, Y. Castin, and J. Dalibard, J. Opt. Soc. Am. B **10**, 524 (1993).

[22] U. Janicke and M. Wilkens, Phys. Rev. A **50**, 3265 (1994).

[23] R. L. Burden and J. D. Faires, *Numerical Analysis* (Brooks/Cole, Florence, KY, 2001), 7th ed.

[24] H. J. Metcalf and P. van der Straten, *Laser Cooling and Trapping* (Springer-Verlag, New York, 1999).

[25] F. K. Fatemi, M. L. Terraciano, M. Bashkansky, and Z. Dutton, Opt. Express **17**, 12971 (2009).

[26] M. Weel and A. Kumarakrishnan, Phys. Rev. A **67**, 061602(R) (2003).

[27] I. S. Gradshteyn and I. M. Ryzhik, *Tables of Integrals, Series, and Products* (Elsevier, Maryland Heights, MO, 2007), 7th ed., p. 940.